Water Science and Engineering 2025, 18(2): 236–246

HOSTED BY

ELSEVIER

Available online at www.sciencedirect.com

Water Science and Engineering

journal homepage: wse.hhu.edu.cn

Three-dimensional numerical simulation of mixing patterns at open channel confluences

Ali Aghazadegan [a,b,*], Ali Shokri [a]

[a] School of Engineering, University of Waikato, Hamilton 3210, New Zealand
[b] School of Engineering, Waikato Institute of Technology, Hamilton 3210, New Zealand

Received 29 December 2023; accepted 30 July 2024
Available online 8 August 2024

Abstract

Open channel confluences, where two streams or rivers converge, play a crucial role in hydraulic engineering and river dynamics. These confluences are characterized by complex hydrodynamics influenced by the discharge ratios of merging water bodies. This study investigated the mixing structure at open channel confluences using three-dimensional numerical modeling. A comprehensive three-dimensional numerical model was developed and validated against a dataset obtained from controlled laboratory experiments. This dataset incorporated three-dimensional time-averaged velocity measurements. The skew-induced and stress-induced equation systems were adopted as the core governing equations, providing a framework for simulating various scenarios. A total of ten different cases were analyzed. The results highlighted the effect of discharge ratios on turbulence, lateral and vertical vorticities, and the distribution of mixing, which intensified with higher magnitudes of discharge ratios. The mixing structure, driven by velocity gradients and vorticity, revealed the significant role of lateral and vertical vorticities in determining hydrodynamic behaviors and mixing distributions at confluences. Specifically, the momentum ratio of incoming flows governed the spatial evolution of mixing processes. This study revealed that the distribution of mixing served as a key indicator for identifying the formation of mid-channel scours. High normalized velocities induced toward the left bank led to the superelevation of the water surface, enhancing the potential for bed material and the formation of significant scour holes beneath the elevated water surface. This novel approach provides a deeper understanding of the mixing patterns at confluences, particularly in scenarios with equilibrated discharge ratios but in different magnitudes.

Keywords: Confluence; Mixing pattern; Numerical modelling; Transverse vorticity; Vertical vorticity

1. Introduction

River confluences, where two or more rivers merge (Jiang et al., 2022; Yuan et al., 2022), are crucial for the studies of hydrodynamics, morphology, and river engineering within drainage basins (Cheng and Constantinescu, 2020; Jiang et al., 2022; Shen et al., 2022; Van der Mark and Mosselman, 2013; Wuppukondur, 2018; Yuan et al., 2021; He et al., 2024). The hydrodynamics of confluences in rivers are usually complex due to the interaction of flows from different rivers and the coverage of streams over extended distances. This interaction generates turbulent eddies and shear layers, which can affect velocity, water surface elevation, and sediment transport at confluences (Best, 1988; Bouchez et al., 2010; Boyer et al., 2006; Konsoer and Rhoads, 2014; Martín-Vide et al., 2015; Nazari-Giglou et al., 2016).

Numerous studies have analyzed the structure of confluences using laboratory experiments, field observations, and numerical simulations. These studies have revealed a three-dimensional (3D) flow structure at confluences, characterized by streamwise coherent structures and enhanced mixing

* Corresponding author.
E-mail addresses: aa323@students.waikato.ac.nz, liam.aghazadegan@wintec.ac.nz (Ali Aghazadegan).
Peer review under responsibility of Hohai University.

https://doi.org/10.1016/j.wse.2024.08.001

dynamics along mixing interfaces. Several researchers (Duguay et al., 2022b, 2023; Gualtieri et al., 2018; Lewis et al., 2020; Middleton et al., 2019; Xie et al., 2018) analyzed flow field data and observed the presence of vorticities and coherent structures that significantly enhance the dynamics between merging tributaries. Sukhodolov et al. (2010) further extended this understanding through a field study measuring mean and turbulent characteristics along the straight reach of a natural river. They focused on the key components of the energy budget and revealed how the lateral fluxes of mean momentum affect the velocity differentials with the shear layers to shape the spatial characteristics of confluences. These findings aligned with those of Constantinescu et al. (2012), who utilized eddy-resolving simulations to specifically examine the formation of mixing interfaces and streamwise-oriented vortical cells at confluences. Cheng and Constantinescu (2020) explored the effects of stratification at a medium-sized stream confluence with discordant bed levels. They analyzed the impacts of temperature differences and resultant density variations, and the simulations demonstrated how stratification alters flow hydrodynamics and enhances thermal mixing, illustrating that even slight temperature changes can lead to significant alterations in flow structures and dynamics. Similarly, Horna-Munoz et al. (2020) investigated the influence of temperature-induced density differences at a small bed confluence through eddy-resolving simulations and found that slight variations in density, driven by temperature differences, significantly affect the development of secondary flows and mixing patterns, thereby enhancing overall mixing efficiency within the confluence zone. Finally, Duguay et al. (2022b) and Lewis et al. (2020) investigated the dynamics of streamwise-orientated vortices at a mesoscale river confluence using aerial drone video analysis and eddy-resolved numerical modeling. They found that these vortices, driven by small density differences between tributaries, are distinct from other flow structures and play a minimal role in lateral mixing within the post-confluence reach, highlighting a specific gravity current effect due to the lateral momentum of converging tributaries.

The pioneering study by Taylor (1944) utilized flume experiments linking tributary and mainstream flows to establish a fundamental correlation between water depth ratios at confluences. Following Taylor (1944), Best (1988) identified six distinct zones characterizing concordant bed confluences: flow stagnation, flow deflection, flow separation, maximum velocity, flow recovery, and shear. Yu et al. (2020) expanded this framework and conducted a detailed laboratory study to analyze the effects of junction angle on flow, secondary flow pattern, and turbulent structure within the confluence zone. They found that junction angle plays a more significant role than discharge ratio in influencing confluence hydrodynamics. Secondary flows and high turbulence are responsible for the formation of mid-channel scour holes. Based on the understanding of secondary flows, Canelas et al. (2022) focused on the strength of secondary circulation within confluences. Their laboratory studies demonstrated that secondary circulation, significantly influenced by factors such as tributary and main flow rates and confluence angle, plays a crucial role in sediment transport and morphological transformations at confluence points. These findings complement the work of Yuan et al. (2023), who explored the effects of floodplain presence on confluence hydrodynamics by comparing two geometric configurations: one with and one without a floodplain in the tributary. The findings revealed that confluences with a floodplain exhibit more intensified secondary motions, a broader separation zone, and overall, more complex flow dynamics than those without a floodplain.

To further deepen our understanding of river confluences, numerous studies have employed numerical models to simulate the complex hydrodynamics and vortices occurring within confluences (Cheng and Constantinescu, 2020; Dong et al., 2023; Duguay et al., 2022a; Jiang et al., 2022; Yuan et al., 2022). Bradbrook et al. (2000) utilized advanced 3D numerical modeling to analyze flow structure generation at confluences. They studied both laboratory settings and field confluence sites such as the Kaskaskia River and Copper Slough and highlighted the presence of time-averaged helical flow structures resembling back-to-back meanders, especially notable in symmetrical “Y-shaped” configurations where two counter-rotating helical cells are produced. However, at asymmetric confluences, the influence of these structures was limited to areas closer to the confluence apex, illustrating how local topography and flow conditions control flow dynamics. Shakibainia et al. (2010) advanced this understanding through the development of a comprehensive 3D numerical model focusing on interactions between tributaries with varying geomorphic attributes. They found that increases in the confluence angle and Froude number, coupled with reductions in discharge and width ratio, lead to an expanded separation zone and a more constricted contraction zone characterized by increased secondary flow. The study also noted the formation of pronounced helical cells and significant variations in water surface levels within the confluence, attributing these phenomena to the distortion of the shear layer caused by differences in streamwise velocities between tributaries. These findings complement the work of Sukhodolov et al. (2010), who found that the lateral fluxes of mean momentum typically decrease mean streamwise velocities at high-velocity layers, highlighting the influence of flow asymmetry on the turbulent transport of momentum within the shear layer. Constantinescu et al. (2011a) further extended this line of inquiry by employing eddy-resolved numerical modeling to predict the formation of streamwise-oriented vortices at a small-scale asymmetrical concordant bed confluence. Their study underscored the dynamic behavior of secondary motions, which are critical in shaping flow structure and sediment transport at confluences. These findings were corroborated by Canelas et al. (2022), who identified a mechanism driving secondary flow at discordant bed confluences with a fixed bed, aligning with earlier observations by Canelas et al. (2020). Riley and Rhoads (2012) and Sukhodolov and Sukhodolova (2019) further explored the effects of changes in momentum−flux ratio on secondary motions, noting that small-scale secondary flow with the same

rotational sense as large-scale helices can develop at the margins of the mixing interface. These secondary motions play a significant role in sediment dynamics and morphological changes at the confluence. Finally, a comprehensive review by Constantinescu (2014) emphasized the efficacy of eddy-resolving techniques, including the large eddy simulation (LES) and hybrid Reynolds-averaged Navier−Stokes (RANS)−LES, in capturing the spatial development and dynamics of mixing interfaces.

Comparing flow fields across different angled confluences with both concordant and deformed bed geometries reveals that geometry significantly affects the formation and dynamics of coherent structures such as streamwise-oriented vortices (SOVs) and mixing interfaces. At confluences with varying angles, the junction geometry, including the concordance or discordance of bed levels and the presence of a floodplain, significantly influences hydrodynamic behaviors, such as the formation of secondary flows, SOV cells, and the extent of mixing. For instance, lower junction angles and minimal curvature enhance SOV development, promoting sediment mobilization even without pronounced bed deformation. Stratification effects, particularly those from temperature-induced density differences, modify flow dynamics, with denser fluids influencing underflow and enhancing mixing efficiency across various confluence configurations. Studies also have highlighted the importance of lateral momentum fluxes and shear layer dynamics, which are affected by the confluence angle and contribute to variations in velocity distributions and turbulence intensities. The presence of a floodplain, as observed in larger river systems, introduces complexity by amplifying secondary motions and expanding separation zones, thereby affecting sediment transport and morphological changes.

Although experimental and numerical studies have been conducted to explore vorticities within the mixing interface and several conceptual models have been employed to investigate the flow structure at channel confluences, the relationship between vorticities and mixing distributions at confluences remains unclear. This study aimed to fill this gap by investigating the impacts of skew-induced and stress-induced turbulence parameters on the dynamics of mixing structures at river confluences. The research approach involved evaluating both transverse and vertical vorticities at open channel confluences using 3D numerical models validated with laboratory data. With skew-induced and stress-induced equations, a range of discharge ratios were explored to determine turbulence parameters that effectively represent the mixing pattern at open channel confluences.

2. Materials and methods

2.1. Numerical model framework

To understand the complex mixing patterns at river confluences, 3D numerical models based on Ansys Fluent and Delft3D-FLOW were utilized. These models have been validated against the findings from laboratory work conducted by Yu et al. (2020) at a 90° confluence.

2.1.1. Ansys Fluent

Ansys Fluent is a comprehensive tool of computational fluid dynamics (CFD) used for modeling fluid flow. It offers advanced features such as turbulent and multiphase flow simulations, a variety of turbulence models, and extensive options for meshing and post-processing.

The volume of fluid (VOF) model is a tool for tracking and locating the free surface (or interface) between two or more unmixable fluids. This feature is particularly useful for simulating open channel flows. The core of the VOF model is the volume fraction equation for each fluid phase. The volume fraction for each cell is defined as the ratio of the volume of a particular fluid to the total volume of the cell. The VOF model solves the continuity equation for the volume fraction of each phase. The $k-\omega$ shear stress transport model is a widely used turbulence model, particularly suitable for complex turbulent flows with adverse pressure gradients and areas of separation, such as those encountered in open channel flows. For the continuity equation for the volume fraction in the VOF model and the governing equations for turbulent kinetic energy and specific rate dissipation, please consult the website of Ansys Fluent (https://www.ansys.com/).

2.1.2. Delft3D-FLOW

Delft3D-FLOW is a 3D numerical model that utilizes the finite difference method on an orthogonal curvilinear grid to solve shallow-water equations. It has been widely used for simulating hydrodynamic and water quality processes in coastal areas, estuaries, and rivers (Deltares, 2024). Delft3D-FLOW simulates flow patterns to derive depth-averaged flow parameters. The governing equations are based on the Navier−Stokes equations and employ Leibniz integration in the vertical direction. Please consult Deltares (2024) for the depth-averaged continuity equation and momentum equations.

2.2. Numerical model setup

The experimental results from Yu et al. (2020), who focused on the accumulation of contaminated sediments, were used for model validation in this study. The experiment involved two channels (Fig. 1). The main channel was 10.0 m long, 0.4 m wide at the post-confluence, and 0.3 m wide in the main section. The tributary channel was 3.0 m long and 0.3 m wide, with a 0.01% bed slope. At 3 m from the main channel intake, the confluence channel joined at a 90° angle to the main channel. Flow discharges were 9 L/s in the main channel and 6 L/s in the tributary channel. Fig. 1 shows the experimental setup for the 90° confluence. Table 1 provides an overview of the boundary conditions used in the numerical model.

The validation of flow dynamics at the river confluence was performed using both Ansys Fluent and Delft3D-FLOW numerical models. The results were compared to the

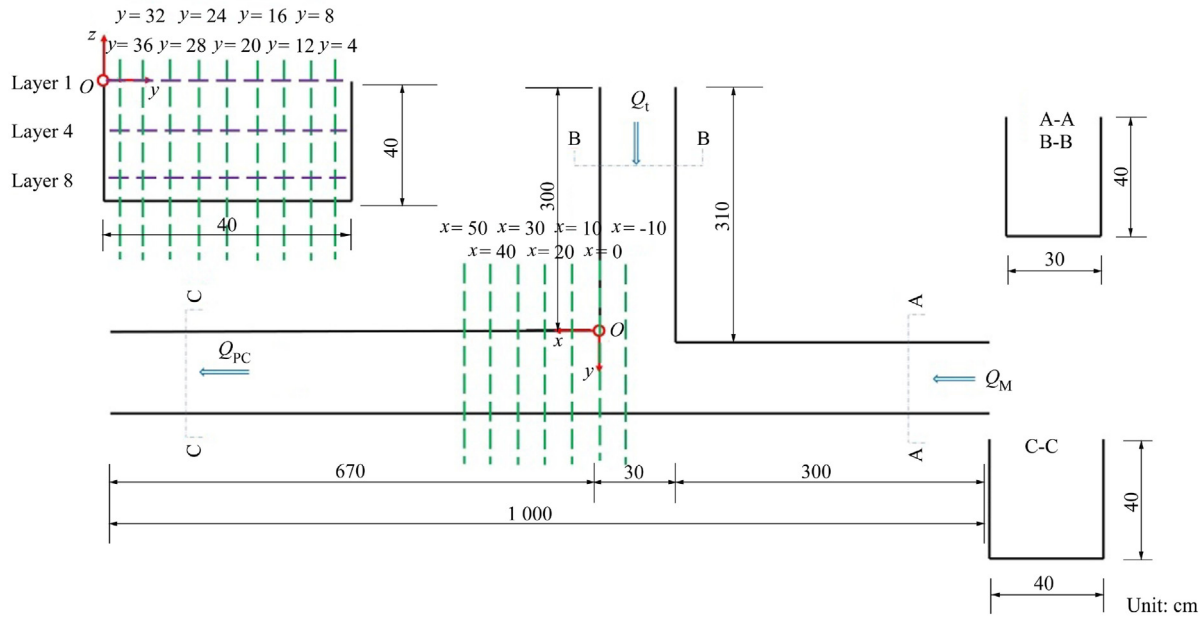

Fig. 1. Experimental setup of 90° confluence (with blue arrows denoting discharge directions, red letters representing cross-sections, and Q_M, Q_t, and Q_{PC} denoting discharges at mainstream, tributary, and post-confluence, respectively).

experimental setup conducted by Yu et al. (2020) at a 90° confluence. The validation analysis, as outlined in Appendix A, indicated that Ansys Fluent accurately simulated the confluence.

Based on a sensitivity analysis, grid sizes of 10 mm × 10 mm in Ansys Fluent and 45 mm × 45 mm in Delft3D-FLOW were utilized. In Ansys Fluent, input boundary conditions were defined by velocity and flow depth, while in Delft3D-FLOW, they were defined by discharge. The outlet boundary condition was set as a fixed water level in both models. Following another sensitivity analysis, a time step of 0.05 min was chosen. In Delft3D-FLOW, the $k-\varepsilon$ turbulence model was used, whereas in Ansys Fluent, various turbulence models such as the Laminar model, the $k-\omega$ model, the Reynolds stress model, and LES were examined.

Table 1
Overview of various model scenarios.

Model No.	Discharge ratio	Momentum ratio	Discharge (L/s)		
			Tributary	Main channel	Post-confluence
M1	2:3	0.60	6.0	9.0	15.0
M2	2:6	0.25	6.0	18.0	24.0
M3	2:9	0.15	6.0	27.0	33.0
M4	1:1	1.00	8.0	8.0	16.0
M5	1:1	1.00	9.0	9.0	18.0
M6	1:1	1.00	12.0	12.0	24.0
M7	4:9	0.37	12.0	27.0	39.0
M8	1:2	0.43	13.5	27.0	40.5
M9	1:1	1.00	18.0	18.0	36.0
M10	2:3	0.61	18.0	27.0	45.0

3. Results

3.1. Time-averaged velocity

To visualize the complex flow dynamics within the confluence zone, the time-averaged velocity fields at cross sections of $x = 10$ cm, $x = 30$ cm, and $x = 50$ cm (where x is the distance on the x axis from the origin) were delineated (Fig. 2). Each figure distinctly illustrates the in-plane velocity components (v and w, where v is the transverse velocity, and w is the vertical velocity) through vector representation, while the streamwise velocity component (u) is depicted using color gradients. At the cross-section positioned at $x = 10$ cm, the flow distinctly separated at the corner, leading to the formation of a recirculation zone (RZ), as shown in Fig. 2(a). This figure further elucidates that the RZ, characterized by $u < 0$, extended throughout the entire water column with pronounced lateral velocity vectors. The cross-sectional analysis at $x = 30$ cm confirmed the persistent presence of the RZ across the full water column, with a noticeable presence of vertical velocity vectors, as shown in Fig. 2(b). The analysis at $x = 50$ cm also confirmed the presence of the RZ, as shown in Fig. 2(c).

3.2. Turbulent kinetic energy

The normalized turbulent kinetic energy (TKE) is used to quantify turbulence intensity and mixing within the flow:

$$E_{TK} = \frac{u'^2 + v'^2 + w'^2}{2U_{PC}^2} \quad (1)$$

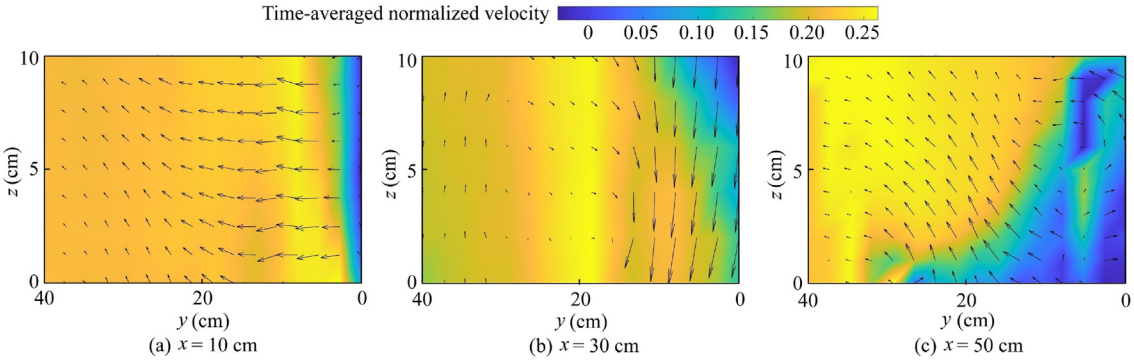

Fig. 2. Time-averaged normalized velocity fields at cross sections of $x = 10$ cm, $x = 30$ cm, and $x = 50$ cm (with color scheme denoting mean streamwise velocity on vertical y–z plane, vector arrows indicating direction and magnitude of velocity vector (v, w) on y–z plane, y denoting distance on y axis from origin, and z representing distance on z axis from origin).

where E_{TK} is the normalized TKE; u', v', and w' are the fluctuating velocity components in the x, y, and z directions, respectively; and U_{PC} is the post-confluence channel velocity.

In the confluence area, high TKE levels correspond to strong velocity gradients and significant mass and momentum mixing between the tributary and main channels, as observed by Bradbrook et al. (1998). Similar to the study by Yu et al. (2020), discharges of 9 and 6 L/s in the main and tributary channels, respectively, were used in the model to illustrate the normalized TKE (Fig. 3).

Fig. 3(a) shows that at the cross section of $x = 10$ cm, there was a noticeable peak of the elevated normalized TKE (depicted in yellow) near the confluence point where the two streams merged. This suggested heightened turbulence at the confluence, due to the merging of different flow regimes. The presence of this peak near the surface indicated that the turbulence generated by the confluence strongly impacted the surface layer, with the turbulent effects of the confluence being highly localized. A gradient of the normalized TKE extending from the confluence point suggested deep dispersion or propagation of turbulence, indicating the expansion of the normalized TKE that could lead to bottom scour. Fig. 3(b) shows that at the cross section of $x = 30$ cm, the high normalized TKE region was located around $y = 20$ cm and $z = 5$ cm. However, the intensity of the normalized TKE decreased slightly compared to the cross section of $x = 10$ cm. The overall distribution of the normalized TKE remained relatively consistent across the channel. Fig. 3(c) shows that at the cross section of $x = 50$ cm, the high turbulent region became even more confined to the area around the water surface. The majority of the cross-section exhibited low normalized TKE values.

Fig. 4 illustrates the contours of the time-averaged velocity within a plane at $z = 10$ cm. The highest velocity magnitudes were observed in the flow contraction zone, which depended upon the size of the adjacent RZ.

Fig. 4(a), characterized by a discharge ratio of 9:6, shows a distinct velocity peak near the confluence from the main channel, highlighting the dominant hydraulic contribution of the main channel. The proximity of the peak velocity to the confluence point demonstrated the dynamic interactions at the junction ($x = 0$ cm and $y = 0$ cm). Fig. 4(b) depicts the scenario with an equilibrated discharge ratio of 8:8. Under this scenario, the peak velocity zone demonstrated a more centralized distribution across the channel compared to the scenario with a discharge ratio of 9:6. The centralization of peak velocities suggested a more evenly distributed momentum, occurring alongside the merging of equal water flows from the main channel and tributary (between $x = 0$ cm and $x = 40$ cm). As shown in Fig. 4(c), with an equilibrated discharge ratio of 9:9, a similar pattern to that of Fig. 4(b) emerged, despite a modestly enhanced spatial extent of velocity downstream of the apex (between $x = 0$ cm and $x = 40$ cm and between $y = 0$ cm and $y \approx 15$ cm). This observation reflected intensified kinetic energy and momentum interchange mechanisms, leading to amplified high-velocity zones. Fig. 4(d), presenting a uniform discharge

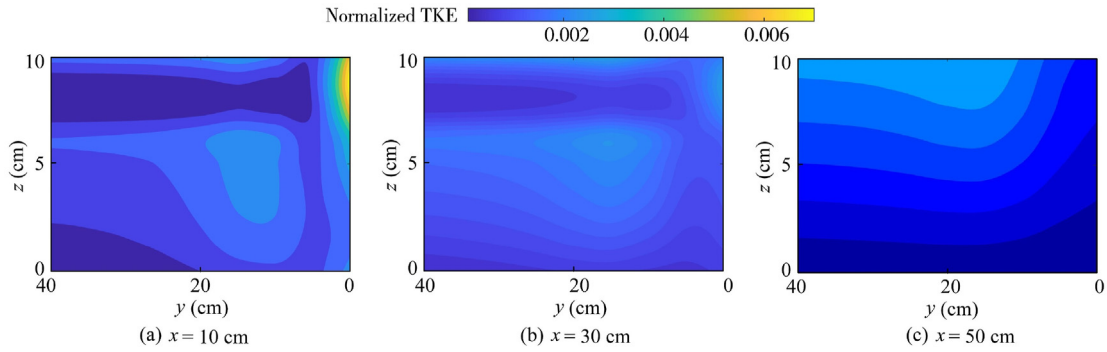

Fig. 3. Normalized TKE at cross sections of $x = 10$ cm, $x = 30$ cm, and $x = 50$ cm.

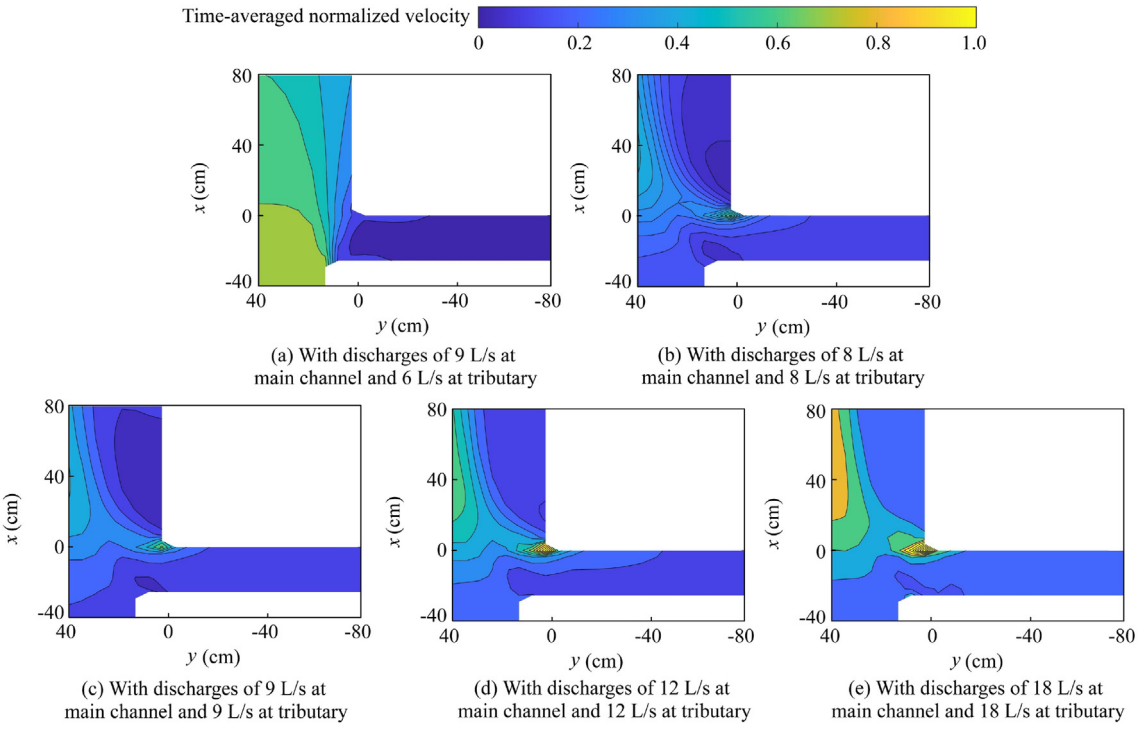

Fig. 4. Time-averaged normalized velocity at $z = 10$ cm with different discharge ratios.

ratio of 12:12, shows that the normalized velocity exhibited a broadening dispersion across the channel, with the enhanced velocity in the area between $x = 0$ cm and $x = 80$ cm and between $y \approx 25$ cm and $y \approx 40$ cm. As shown in Fig. 4(e), with the highest equilibrated discharge ratio of 18:18, a significant transition occurred. The high-velocity zones demonstrated significant spatial expansion, with the velocity distribution covering the entire width of the channel. The velocity enhancement continued in the area between $x = 0$ cm and $x = 80$ cm and between $y \approx 25$ cm and $y \approx 40$ cm. This observation led to superelevation at the outer bank of the confluence, inducing a strong downwelling of fluid at the outer bank of the open channel.

3.3. Skew-induced mechanism

The skew-induced mechanism, known as Prandtl's first type of secondary flow, is produced through the quasi-deflection of the existing mean vorticity (Canelas et al., 2022). The deflection is represented by the two terms ($\omega_y \partial U/\partial y$ and $\omega_z \partial U/\partial z$) in Eq. (2):

$$\overbrace{U\frac{\delta\omega_x}{\delta x}+V\frac{\delta\omega_x}{\delta y}+W\frac{\delta\omega_x}{\delta z}}^{A}=\overbrace{\omega_x\frac{\delta U}{\delta x}+\omega_y\frac{\delta U}{\delta y}+\omega_z\frac{\delta U}{\delta z}}^{B}+\overbrace{\left(\frac{\partial^2}{\partial y^2}-\frac{\partial^2}{\partial z^2}\right)(-\overline{uw})}^{C}+\overbrace{\frac{\partial^2}{\partial y\partial z}\left(\overline{v^2}-\overline{w^2}\right)}^{D}+\overbrace{\vartheta\nabla^2\omega_x}^{E} \tag{2}$$

where U, V, and W are the time-averaged velocity components in the x, y, and z directions, respectively; u, v, and w are the fluctuating velocity components based on the Reynolds decomposition in the x, y, and z directions, respectively; ϑ is the kinematic viscosity; and ω_x, ω_y, and ω_z are the streamwise, crosswise, and vertical vorticities, respectively, defined as $\omega_x = \partial W/\partial y - \partial V/\partial z$, $\omega_y = \partial U/\partial z - \partial W/\partial x$, and $\omega_z = \partial V/\partial x - \partial U/\partial y$, respectively. This mechanism applies irrespective of whether the secondary vorticity forms distinct streamwise vortices or is spread across the shear layer in a typical 3D boundary layer. $\omega_y \partial U/\partial y$ and $\omega_z \partial U/\partial z$ represent the generation of vortices caused by the quasi-inviscid deflection of the mean vorticity. In Eq. (2), term B describes the amplification of ω_x by vortex stretching, while ω_y and ω_z are related to the skew-induced generation of vorticities through the deflection of the existing mean vorticity. Terms C and D involve Reynolds stresses and the relative sizes of normal stresses, which may be responsible for the stress-induced generation of vorticities.

3.4. Stress-induced mechanism

The stress-induced mechanism, known as Prandtl's second type of secondary flow, is generated by turbulent (Reynolds) stresses, with the directions of y and z axes determine the respective magnitudes of the normal stress and shear stress contributions. Secondary flow patterns in the y–z plane are related to the following two types: (1) crossflow, which occurs in a thin shear layer or a 3D boundary layer when the axial vorticity ($\partial W/\partial y - \partial V/\partial z$) is almost entirely contained in $\partial W/\partial y$; and (2) identifiable streamwise vortices, in which $\partial W/\partial y$ is roughly equivalent to $\partial V/\partial z$. Shear layer development was evaluated based on the components of vortex stretching (term B in Eq. (2)), the crossflow components of mean vorticities (ω_x, ω_y, and ω_z), and streamwise velocity derivatives ($\partial U/\partial x$, $\partial U/\partial y$, and $\partial U/\partial z$).

Fig. 5 provides a quantified representation of the spatial variation of terms in Eq. (2) within the confluence zone. The evaluation of the secondary circulation, both within and downstream of the tributary mouth, relies on the measurements of the mean vorticity components: streamwise, crosswise, and vertical. Additionally, the assessment depends on the streamwise velocity derivatives, and the components of vortex stretching.

Fig. 5(a) shows that the streamwise velocity derivative (du/dx) captured the gradient of the streamwise velocity along the x axis. The figure highlights the regions with significant streamwise velocity differentiation, especially near the apex where the tributary flow met the main channel, marked by an intensified velocity gradient. Further downstream along the x axis, a noticeable distribution of the transverse velocity gradient across the spanwise channel width (y) appeared in the area between $x = 0$ cm and $x = 80$ cm and between $y = 0$ cm and $y \approx 10$ cm. This distribution indicated that the tributary inflow to the main channel affected the downstream streamwise velocity profile.

Fig. 5(b) provides a visualization of the transverse velocity gradient (dv/dy) within the confluence. As the contours extend across the spanwise (y) and streamwise (x) dimensions of the channel, a gradational transition from high to low gradients was observed. The gradient suggested that a decrease in transverse velocity changes advanced downstream, specifically in the area between $x \approx -30$ cm and $x = 80$ cm and between $y \approx -5$ cm and $y \approx 25$ cm. This observation aligned with the findings of Lyubimova et al. (2020) in an idealized rectangular channel.

Fig. 5(c) shows the vertical velocity derivative (dw/dz), revealing variations in velocity along the vertical (z) direction.

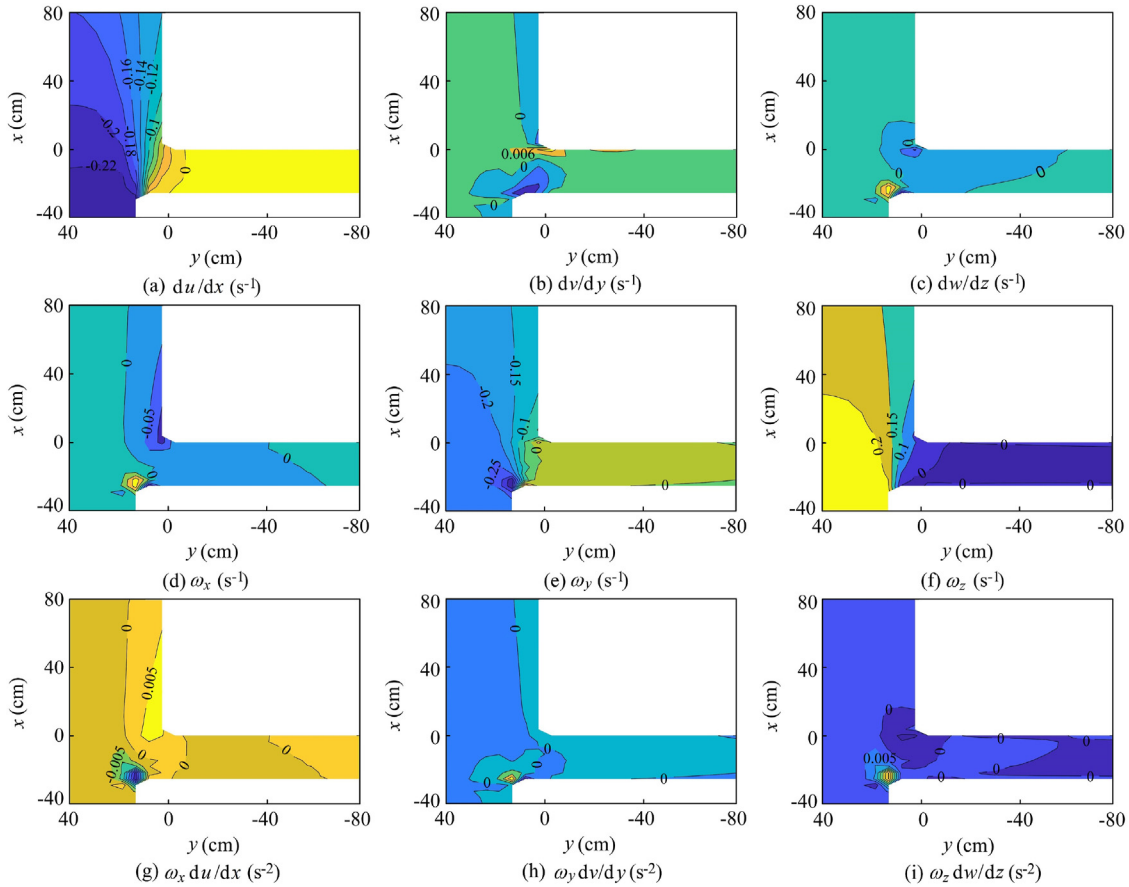

Fig. 5. Spatial distributions of streamwise velocity derivative (du/dx), transverse velocity derivative (dv/dy), vertical velocity derivative (dw/dz), streamwise vorticity (ω_x), transverse vorticity (ω_y), vertical vorticity (ω_z), streamwise vortex stretching (ω_xdu/dx), cross-flow vortex stretching (ω_ydv/dy), and vertical vortex stretching (ω_zdw/dz).

The figure highlights significant vertical momentum transfer. This was particularly evident in the vicinity of the confluence, where interactions between different water flows resulted in significant vertical mixing and either upwelling or downwelling, particularly in the area between $y \approx 0$ cm and $y \approx 15$ cm. The tilting of high-speed flows at the confluence generated negative vorticities, indicating areas with downward water movement. This phenomenon was especially notable near the confluence apex, suggesting that turbulence intensified in this region. The observed velocity gradients indicated the presence of complex flow structures, including the zones of upwelling and downwelling, which play a crucial role in the mixing processes at the confluence. Furthermore, the distribution of these gradients demonstrated a widening of vertical velocity variations along the longitudinal (x) axis, indicating a downstream spread of the vertical momentum from $x \approx 15$ cm.

Fig. 5(d) shows the spatial distribution of the streamwise vorticity (ω_x) within the confluence. The figure reveals a pronounced region of high streamwise vorticity proximal to the confluence, characterized by a sharp transition indicative of a substantial deviation in rotational flow patterns where the tributary met the main channel. The distribution of ω_x across the channel exhibited a discernible propagation of vortical structures downstream (from $x \approx 40$ cm). The streamwise vorticity contours expand and relax in intensity, reflecting the downstream evolution and diffusion of vortical flow. The lateral dispersion of ω_x (along the y axis) showed intense vorticity occurring close to the interface of the merging flows, indicating a lateral confinement of the flow's rotational features, with the greatest impact of streamwise vorticity confined to a limited spanwise region within the vicinity of the tributary.

As shown in Fig. 5(e), the cross-flow vorticity (ω_y) presented pronounced high ω_y values near the confluence point. This accumulation reflected the presence of significant lateral shear forces resulting from the complex merging of the tributary and main channel flows. The spread along the x direction signified the relaxation and diffusion of lateral flow structures. Lateral to the main flow (along the y axis), the distribution of ω_y highlighted the localized impact of the tributary inflow on the transverse dynamics of the confluence. This non-uniformity in the spanwise direction underscored the influence of the tributary, disrupting lateral homogeneity and creating a varied transverse flow pattern.

Fig. 5(f) presents the vertical vorticity (ω_z), which shows a significant concentration of vertical vorticity near the confluence. The gradient in vorticity intensified near the junction, indicating dynamic flow interactions in the area where the tributary and main channel met. The presence of high ω_z values in this region was characteristic of zones where the merging flow paths induced substantial vertical circulation and potential turbulence. The spatial distribution of ω_z showed a distinct expansion away from the confluence point along the streamwise (x) axis. This observation suggested the downstream advection and diffusion of vorticity, reflecting the evolving nature of flow structures as ω_z integrated with the main channel flow.

Fig. 5(g) through (i) presents vortex stretching components. As shown in Fig. 5(g), the streamwise vortex stretching ($\omega_x \mathrm{d}u/\mathrm{d}x$) highlighted the interaction between vorticity and its spatial gradient along the x axis. The transverse vortex stretching ($\omega_y \mathrm{d}v/\mathrm{d}y$) (Fig. 5(h)) underlined the relationship between vorticity and its streamwise gradient the along y axis. Fig. 5(i) highlights that the vertical vortex stretching ($\omega_z \mathrm{d}w/\mathrm{d}z$) significantly intensified in the region closer to the confluence apex.

Fig. 6 shows the variations in transverse vorticity (ω_y) and vertical vorticity (ω_z) across a series of discharge ratios within the confluence zone. Although Fig. 6(a) and (c) adopts equilibrated discharge ratios (8:8 and 9:9, respectively), the transverse vorticity (ω_y) shown in these two figures demonstrated distinctive patterns of lateral flow interactions. As the discharge ratio was increased, the vorticity contours not only amplified but also broadened, indicating more vigorous and far-reaching flow mixing within the main channel dynamics. The intensity and extent of this mixing were further emphasized for the discharge ratios of 12:12 and 18:18 (Fig. 6(e) and (g)). Particularly in Fig. 6(g), the extent of ω_y was significantly magnified, and the transverse vorticity dominated a substantial section of the channel, denoting a significant boost in lateral mixing and momentum transfer.

As shown in Fig. 6(b), (d), (f), and (h), the vertical vorticity (ω_z) with discharge ratios of 8:8, 9:9, 12:12, and 18:18 captured the evolution of vertical mixing. The transition of the discharge ratio from 8:8 to 18:18 underscored a clear trend: the intensification of mixing flow structures within the confluence. This trend was characterized by the enlargement of areas exhibiting high gradients, indicating increasingly vigorous mixing within the confluence zone. The enhanced mixing efficiency was attributed to the momentum exchange between the converging streams, which could significantly affect sediment transport dynamics, including the potential for scour and deposition processes.

4. Discussion

A comprehensive analysis of the spatial distributions and dynamic interactions between merging flows revealed the significant influence of confluence discharge ratios on the extend of mixing processes and flow structures within confluences. The spatial evolution of mixing structures is primarily determined by the momentum ratio of incoming flows (Constantinescu et al., 2012; Sukhodolov and Sukhodolova, 2019). Our findings indicated that the magnitudes of these ratios significantly affected the spatial evolution of mixing processes. For instance, Figs. 2(a) and 4 demonstrate induced high normalized velocities toward the left bank, leading to the superelevation of the water surface (Bradbrook et al., 1998, 2000; De Serres et al., 1999). This superelevation induced a strong downwelling of fluid on the outer bank of the open channel (Fig. 2(a)) and penetrated close to the channel, enhancing the potential for entrainment of bed material and contributing to the formation of a large scour hole beneath the superelevation. Approaching the bed, the descending fluid initially moved laterally away from the outer bank (Fig. 2(b))

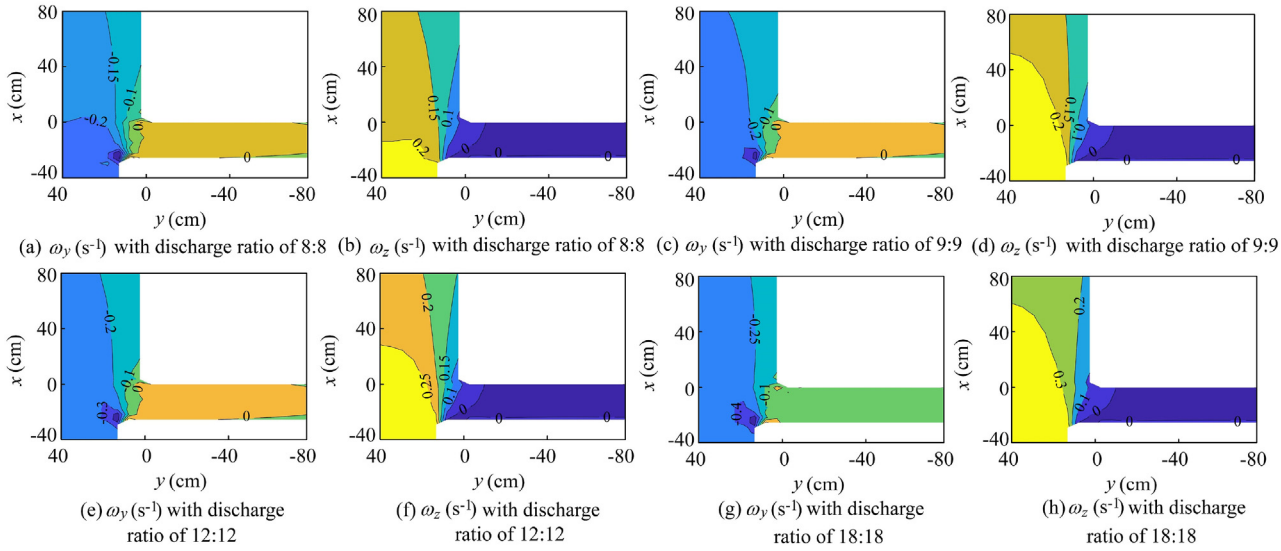

Fig. 6. Spatial distributions of transverse vorticity and vertical vorticity across a confluence zone with discharge ratios 8:8, 9:9, 12:12, and 18:18.

and then ascended toward the free surface. This process led to the spatial evolution of both transverse and vertical vorticities (Fig. 6) and demonstrated significant variability with changes in inflow conditions, even though the discharge ratio remained the same. The transverse vorticity of -0.1 s^{-1} expanded streamwise downstream close to $x = 40$ cm (Fig. 6(a)) but concentrated close to the confluence apex ($x = 0$ cm) as the discharge magnitude was increased (Fig. 6(a), (c), (e), and (g)). When the discharge ratio was increased, there was an increase in the velocity gradient, thereby enhancing the generated vorticity. This was evident from the increasing spread of the vorticity contour of -0.1 s^{-1} as the magnitude of the discharge ratio was increased from 8:8 to 18:18. Additionally, at higher magnitudes of discharge ratios, the interaction between the flow and boundaries (such as walls or obstacles) became more significant, affecting the distribution of vorticity due to the no-slip condition and the generation of boundary layers. Vertical vorticity was also more pronounced close to the confluence apex as the magnitude of the discharge ratio was increased (Fig. 6(b), (d), (f), and (h)). The interaction between the incoming flows resulted in the tilting of vorticity, which are the key mechanisms in the production and evolution of vortical structures. The evaluation of vertical vorticity showed a significant spread across the flow field, extending into both incoming flows. This implied that a higher magnitude of the discharge ratio led to extensive mixing. The transverse and vertical mixing processes effectively transported suspended sediment downstream. The spatial evolution of mixing was consistent with previous theoretical and experimental studies in rectangular channels with flatbeds Canelas et al. (2022); Paola (1997). Previous studies (Constantinescu et al., 2011b; Lewis et al., 2020; Rhoads and Kenworthy, 1999; Rhoads and Sukhodolov, 2001) have measured both two-dimensional and 3D velocity components and identified a region of reduced velocities between the high-velocity cores of incoming flows at cross-sections in the upstream portions of confluences. Despite secondary currents being identified as a crucial factor for rapid mixing, our numerical simulation results indicated that they alone were not a sufficient condition for effective mixing. Within the confluence, the mixing appeared almost vertically uniform near the junction, with secondary flows largely confined to the ambient flow at the edges of the mixing, contributing minimally to the mixing process (Chen et al., 2017; Duguay et al., 2023; Sukhodolov et al., 2010). Only beyond the contraction zone, as the flow moved downstream, both transverse and vertical vorticities developed and enhanced mixing, coinciding with a wide range of intermodal growth dynamics of the mixing interface. This observation aligned with recent studies by Cheng and Constantinescu (2022), Shin et al. (2023), and Sukhodolov et al. (2023).

Our observations further indicated a significant peak in the normalized TKE at the confluence point, particularly near the surface. This was corroborated by the gradient of the normalized TKE extending from the confluence, indicating the potential for deep dispersion and subsequent effects on bottom scour and sediment transport. The velocity magnitudes within the flow contraction zone, as well as the distributions of streamwise, transverse, and vertical velocity gradients, underscores the complex dynamics. The discharge ratio significantly influences these dynamics, with equilibrated ratios leading to more symmetrical momentum distributions and the intensification of kinetic energy and momentum interchange mechanisms. This suggests that the uniformity of discharge rates across tributaries and main channels plays a crucial role in shaping flow characteristics and mixing processes within confluences.

5. Conclusions

This study utilized stress-induced mechanisms and numerical simulations to investigate the spatial evolution of

mixing structures at an open channel confluence with concordant bed morphology under varying inflow conditions. Unlike most previous studies, this research employed equilibrated discharge ratios with different magnitudes and examined both transverse and vertical vorticities. With 3D numerical simulations validated against laboratory data, this study evaluated mean velocity, TKE, and velocity gradient and vorticity structures across various cross-sections and discharge ratios. This study revealed that discharge ratios significantly influenced the mixing processes and flow structures within confluences. Higher discharge ratios led to increased velocity gradients, enhanced vorticity, and extensive mixing, thereby affecting sediment transport and bed material entrainment. Numerical simulations showed that transverse and vertical vorticities developed downstream, highlighting the importance of the magnitude of discharge rates across tributaries for effective mixing and flow dynamics. The novel approach employed in this study provides a deeper understanding of mixing structures at confluences by examining vorticities, especially in scenarios with equilibrated discharge ratios but in different magnitudes.

Declaration of competing interest

The authors declare no conflicts of interest.

Appendix A. Supplementary data

Supplementary data to this article can be found online at https://doi.org/10.1016/j.wse.2024.08.001.

References

Best, J.L., 1988. Sediment transport and bed morphology at river channel confluences. Sedimentology 35(3), 481−498. https://doi.org/10.1111/j.1365-3091.1988.tb00999.x.

Bouchez, J., Lajeunesse, E., Gaillardet, J., France-Lanord, C., Dutra-Maia, P., Maurice, L., 2010. Turbulent mixing in the Amazon River: The isotopic memory of confluences. Earth Planet Sci. Lett. 290(1−2), 37−43. https://doi.org/10.1016/j.epsl.2009.11.054.

Boyer, C., Roy, A.G., Best, J.L., 2006. Dynamics of a river channel confluence with discordant beds: Flow turbulence, bed load sediment transport, and bed morphology. J. Geophys. Res. Earth Surf. 111(4), 1−22. https://doi.org/10.1029/2005JF000458.

Bradbrook, K.F., Biron, P.M., Lane, S.N., Richards, K.S., Roy, A.G., 1998. Investigation of controls on secondary circulation in a simple confluence geometry using a three-dimensional numerical model. Hydrol. Process. 12(8), 1371−1396. https://doi.org/10.1002/(SICI)1099-1085(19980630)12:8<1371::AID-HYP620>3.0.CO;2-C.

Bradbrook, K.F., Lane, S.N., Richards, K.S., 2000. Numerical simulation of three-dimensional, time-averaged flow structure at river channel confluences. Water Resour. Res. 36(9), 2731−2746. https://doi.org/10.1029/2000WR900011.

Canelas, O.B., Ferreira, R.M.L., Guillén-Ludeña, S., Alegria, F.C., Cardoso, A.H., 2020. Three-dimensional flow structure at fixed 70° open-channel confluence with bed discordance. J. Hydraul. Res. 58(3), 434−446. https://doi.org/10.1080/00221686.2019.1596988.

Canelas, O.B., Ferreira, R.M.L., Cardoso, A.H., 2022. Hydro-morphodynamics of an open-channel confluence with bed discordance at dynamic Equilibrium. Water Resour. Res. 58(1), e2021WR029631. https://doi.org/10.1029/2021WR029631.

Chen, X., Zhu, D.Z., Steffler, P.M., 2017. Secondary currents induced mixing at channel confluences. Can. J. Civ. Eng. 44(12), 1071−1083. https://doi.org/10.1139/cjce-2016-0228.

Cheng, Z., Constantinescu, G., 2020. Stratification effects on hydrodynamics and mixing at a river confluence with discordant bed. Environ. Fluid Mech. 20(4), 843−872. https://doi.org/10.1007/s10652-019-09725-6.

Cheng, Z., Constantinescu, G., 2022. Shallow mixing interfaces between parallel streams of unequal densities. J. Fluid Mech. 945, A2. https://doi.org/10.1017/jfm.2022.505.

Constantinescu, G., Koken, M., Zeng, J., 2011a. The structure of turbulent flow in an open channel bend of strong curvature with deformed bed: Insight provided by detached eddy simulation. Water Resour. Res. 47(5), W05515. https://doi.org/10.1029/2010WR010114.

Constantinescu, G., Miyawaki, S., Rhoads, B., Sukhodolov, A., Kirkil, G., 2011b. Structure of turbulent flow at a river confluence with momentum and velocity ratios close to 1: Insight provided by an eddy-resolving numerical simulation. Water Resour. Res. 47(5), W05507. https://doi.org/10.1029/2010WR010018.

Constantinescu, G., Miyawaki, S., Rhoads, B., Sukhodolov, A., 2012. Numerical analysis of the effect of momentum ratio on the dynamics and sediment-entrainment capacity of coherent flow structures at a stream confluence. J. Geophys. Res. Earth Surf. 117, F04028. https://doi.org/10.1029/2012jf002452.

Constantinescu, G., 2014. LE of shallow mixing interfaces: A review. Environ. Fluid Mech. 14(5), 971−996. https://doi.org/10.1007/s10652-013-9303-6.

De Serres, B., Roy, A.G., Biron, P.M., Best, J.L., 1999. Three-dimensional structure of flow at a confluence of river channels with discordant beds. Geomorphology 26(4), 313−315. https://doi.org/10.1016/s0169-555x(98)00064-6.

Deltares, 2024. Simulation of Multi-dimensional Hydrodynamic Flows and Transport Phenomena, Including Sediments. Deltares, Delft, Version 4.05. .

Dong, S., Wei, D., Cai, Y., Wang, B., Cheng, T., Zhang, Y., 2023. Experimental and numerical study on the performance and mechanism of a vortex-broken electrocyclone. Chem. Eng. J. 455, 140758. https://doi.org/10.1016/j.cej.2022.140758.

Duguay, J., Biron, P., Buffin-Bélanger, T., 2022a. Large-scale turbulent mixing at a mesoscale confluence assessed through drone imagery and eddy-resolved modelling. Earth Surf. Process. Landforms 47(1), 345−363. https://doi.org/10.1002/esp.5251.

Duguay, J., Biron, P.M., Lacey, J., 2022b. Aerial observations and numerical simulations confirm density-driven streamwise vortices at a river confluence. Water Resour. Res. 58(7), e2021WR031527. https://doi.org/10.1029/2021WR031527.

Duguay, J.M., Biron, P.M., Lacey, R.W.J., 2023. Density effects on streamwise-orientated vorticity at river confluences: A laboratory investigation. J. Fluid Mech. 973, 1−30. https://doi.org/10.1017/jfm.2023.656.

Gualtieri, C., Filizola, N., de Oliveira, M., Santos, A.M., Ianniruberto, M., 2018. A field study of the confluence between Negro and Solimões rivers. Part 1: Hydrodynamics and sediment transport. Compt. Rendus Geosci. 350(1−2), 31−42. https://doi.org/10.1016/j.crte.2017.09.015.

He, W., Feng, S., Zhang, J., Tang, H., Xiao, Y., Chen, S., Liu, C., 2024. Hydrodynamic characteristics and particle tracking of 90° lateral intakes at an inclined river slope. Water Sci. Eng. 17(2), 197−208. https://doi.org/10.1016/j.wse.2023.11.004.

Horna-Munoz, D., Constantinescu, G., Rhoads, B., Lewis, Q., Sukhodolov, A., 2020. Density effects at a concordant bed natural river confluence. Water Resour. Res. 56(4), e2019WR026217. https://doi.org/10.1029/2019WR026217.

Jiang, C., Constantinescu, G., Yuan, S., Tang, H., 2022. Flow hydrodynamics, density contrast effects and mixing at the confluence between the Yangtze River and the Poyang Lake channel. Environ. Fluid Mech. 23, 229−257. https://doi.org/10.1007/s10652-022-09848-3.

Konsoer, K.M., Rhoads, B.L., 2014. Spatial−temporal structure of mixing interface turbulence at two large river confluences. Environ. Fluid Mech. 14(5), 1043−1070. https://doi.org/10.1007/s10652-013-9304-5.

Lewis, Q., Rhoads, B., Sukhodolov, A., Constantinescu, G., 2020. Advective lateral transport of streamwise momentum governs mixing at small river confluences. Water Resour. Res. 56(9), e2019WR026817. https://doi.org/10.1029/2019WR026817.

Lyubimova, T.P., Lepikhin, A.P., Parshakova, Y.N., Kolchanov, V.Y., Gualtieri, C., Roux, B., Lane, S.N., 2020. A numerical study of the influence of channel-scale secondary circulation on mixing processes downstream of river junctions. Water 12(11), 2969. https://doi.org/10.3390/w12112969.

Martín-Vide, J.P., Plana-Casado, A., Sambola, A., Capapé, S., 2015. Bedload transport in a river confluence. Geomorphology 250, 15−28. https://doi.org/10.1016/j.geomorph.2015.07.050.

Middleton, L., Ashmore, P., Leduc, P., Sjogren, D., 2019. Rates of planimetric change in a proglacial gravel-bed braided river: Field measurement and physical modelling. Earth Surf. Process. Landforms 44(3), 752−765. https://doi.org/10.1002/esp.4528.

Nazari-Giglou, A., Jabbari-Sahebari, A., Shakibaeinia, A., Borghei, S.M., 2016. An experimental study of sediment transport in channel confluences. Int. J. Sediment Res. 31(1), 87−96. https://doi.org/10.1016/j.ijsrc.2014.08.001.

Paola, C., 1997. When streams collide. Nature 387(6630), 232−233. https://doi.org/10.1038/387232a0.

Rhoads, B.L., Kenworthy, S.T., 1999. On secondary circulation, helical motion and Rozovskii-based analysis of time-averaged two-dimensional velocity fields at confluences. Earth Surf. Process. Landforms 24(4), 369−375. https://doi.org/10.1002/(SICI)1096-9837(199904)24:4<369::AID-ESP983>3.0.CO;2-F.

Rhoads, B.L., Sukhodolov, N., 2001. Field investigation of three-dimensional flow structure. Water Resour. Res. 37(9), 2393−2410. https://doi.org/10.1029/2001WR000316.

Riley, J.D., Rhoads, B.L., 2012. Flow structure and channel morphology at a natural confluent meander bend. Geomorphology 163−164, 84−98. https://doi.org/10.1016/j.geomorph.2011.06.011.

Shakibainia, A., Tabatabai, M.R.M., Zarrati, A.R., 2010. Three-dimensional numerical study of flow structure in channel confluences. Can. J. Civ. Eng. 37(5), 772−781. https://doi.org/10.1139/L10-016.

Shen, X., Li, R., Cai, H., Feng, J., Wan, H., 2022. Characteristics of secondary flow and separation zone with different junction angle and flow ratio at river confluences. J. Hydrol. 614, 128537. https://doi.org/10.1016/j.jhydrol.2022.128537.

Shin, J., Lee, S., Park, I., 2023. Influences of momentum ratio on transverse dispersion for intermediate-field mixing downstream of channel confluence. Int. J. Environ. Res. Publ. Health 20(4), 2776. https://doi.org/10.3390/ijerph20042776.

Sukhodolov, A.N., Schnauder, I., Uijttewaal, W.S.J., 2010. Dynamics of shallow lateral shear layers: Experimental study in a river with a sandy bed. Water Resour. Res. 46(11), W11519. https://doi.org/10.1029/2010WR009245.

Sukhodolov, A.N., Sukhodolova, T.A., 2019. Dynamics of flow at concordant gravel bed river confluences: Effects of junction angle and momentum flux ratio. J. Geophys. Res. Earth Surf. 124(2), 588−615. https://doi.org/10.1029/2018JF004648.

Sukhodolov, A.N., Shumilova, O.O., Constantinescu, G.S., Lewis, Q.W., Rhoads, B.L., 2023. Mixing dynamics at river confluences governed by intermodal behaviour. Nat. Geosci. 16(1), 89−93. https://doi.org/10.1038/s41561-022-01091-1.

Taylor, E.H., 1944. Flow characteristics at rectangular open-channel junctions. Trans. Am. Soc. Civ. Eng. 109(1), 893−902. https://doi.org/10.1061/TACEAT.0005772.

Van der Mark, C.F., Mosselman, E., 2013. Effects of helical flow in one-dimensional modelling of sediment distribution at river bifurcations. Earth Surf. Process. Landforms 38(5), 502−511. https://doi.org/10.1002/esp.3335.

Wuppukondur, A., 2018. Review of flow hydrodynamics and sediment transport at open channel confluences. Civil Engineering Research Journal 5(3), 555664. https://doi.org/10.19080/cerj.2018.05.555664.

Xie, Q., Yang, J., Lundström, S., Dai, W., 2018. Understanding morphodynamic changes of a tidal river confluence through field measurements and numerical modeling. Water 10(10), 1424. https://doi.org/10.3390/w10101424.

Yu, Q., Yuan, S., Rennie, C.D., 2020. Experiments on the morphodynamics of open channel confluences: Implications for the accumulation of contaminated sediments. J. Geophys. Res. Earth Surf. 125(9), e2019JF005438. https://doi.org/10.1029/2019JF005438.

Yuan, S., Tang, H., Li, K., Xu, L., Xiao, Y., Gualtieri, C., Rennie, C., Melville, B., 2021. Hydrodynamics, sediment transport and morphological features at the confluence between the Yangtze River and the Poyang Lake. Water Resour. Res. 57(3), e2020WR028284. https://doi.org/10.1029/2020WR028284.

Yuan, S., Xu, L., Tang, H., Xiao, Y., Gualtieri, C., 2022. The dynamics of river confluences and their effects on the ecology of aquatic environment: A review. J. Hydrodyn. 34(1), 1−14. https://doi.org/10.1007/s42241-022-0001-z.

Yuan, S., Yan, G., Tang, H., Xiao, Y., Rahimi, H., Aye, M.N., Gualtieri, C., 2023. Effects of tributary floodplain on confluence hydrodynamics. J. Hydraul. Res. 61(4), 552−572. https://doi.org/10.1080/00221686.2023.2231413.